• Article •

SoSpider: A bio-inspired multimodal untethered soft hexapod robot for planetary lava tube exploration

NIU Lizhou[1], DING Liang [1*], ZHANG Shengjie[1], YANG Huaiguang[1], GAO Haibo[1], DENG Zongquan[1], LIU Guangjun[2], Mokarram Hossain[3]

[1]*State Key Laboratory of Robotics and Systems, Harbin Institute of Technology, Harbin 150001, China;*
[2]*Department of Aerospace Engineering, Ryerson University, Toronto, ON M5B 2K3, Canada;*
[3]*Zienkiewicz Institute for Modelling, Data and AI, Swansea University, Swansea, SA1 8EN, United Kingdom.*

Received April 30, 2023, accepted September xx, 2023; published online xx, 2023

Soft robots have tremendous potential for applications in various fields, owing to their safety and flexibility embedded at the material level. Soft robots, especially bio-inspired soft legged robots, have become one of the most active fields of current research in robotics thanks to their superior mobility and ability to face complex terrains. However, it is arduous to establish a dynamic simulation model for soft robots, owing to their hyper-redundant degrees of freedom, hyper-elasticity, and nonlinearity of their soft structures. In this study, we designed, simulated, and fabricated a hexapod robot that achieves walking, crawling, pronking, and rolling with wheeled legs plus a soft body capable of shape change. A robot prototype was fabricated using 3D printing technology and soft silicone pneumatic networks. Actuators, battery power, and control boards were integrated into the body of the robot for untethered locomotion. We have explored the capabilities of the robot in different conditions, especially in scenarios that simulate lunar and Martian environments, demonstrating the motion performance of the robot. The results have shown promising potentials of the developed robot for future applications in planetary lava tube exploration. Our experimental and simulation results also show good agreements that indicate the potential predictive roles of simulation tools for soft robot design, planning, and control.

multimodal, soft robot, pneumatic, simulation, planetary exploration

Citation: Niu L Z, Ding L, Zhang S J. SoSpider: A bio-inspired multimodal untethered soft hexapod robot for planetary lava tube exploration. Sci China Tech Sci, 2016, 59: 183–190, doi: 10.1007/s11431-015-5920-2

1 Introduction

Legs and wheels are most commonly employed in mobile robots. Legged robots have superior terrestrial mobility for traversing diverse environments and thus have the potential to be deployed in outer space or disaster scenes [1]. On the other hand, rolling is the fastest and most energy-efficient gait on flat ground among the motion patterns. The rolling motion generates relatively high speeds and conserves momentum, especially with the help of gravity [2]. Besides, wheeled mobile robots are still primarily used in planetary exploration, and they are among the most intelligent space systems that synergistically combine robotic intelligence, virtual intelligence, and human intelligence [3]. However, they are almost always rigid structures and have a limited exploration area to reach.

At present, both rigid robots and soft robots have their advantages and disadvantages. A rigid mobile robot has high structural stiffness and large load capacity, while it may not be able to pass through narrow caves or crevices. On the contrary, soft mobile robots can take advantage of their softness, easy deformation, and high degrees of freedom to adapt to various unknown and complex environments for undertaking reconnaissance, rescue, and other hazardous tasks. However, design, modeling, and simulation of soft robots are still at their early stage, owing to their hyper-redundant degrees of

freedom, hyper-elasticity, and nonlinearity of the underlying soft materials. It is rare to find reported research on untethered rigid-flexible coupled mobile robots. For future lava cave exploration missions on the Moon and Mars and the scientific exploration of other distant planets, we need to adapt to the harsh space environments and face much more complex and arduous unknown terrains [4]. Developing a multimodal robot that can adapt to different terrain environments is desirable.

Bio-inspired soft locomotion robots exhibit great potential in the fields of measurement, detection, and rescue. Many biological organisms, including species of spiders, salamanders, and caterpillars, change their shapes to switch gaits and adapt to different environments or escape from natural enemies and dangers. When attacked by its nemesis, the predatory wasp, a wheel spider turns its body into a wheel after a short run and rolls down a dune [5]. Similarly, the caterpillar of the mother-of-pearl moth (*Pleurotya ruralis*) rolls into the shape of a wheel and can roll up to five consecutive revolutions to escape any predation [2]. Inspired by such a change, Lin et al. have created GoQbot [6], and Western et al. proposed Spider Rolling Robot (SSR, Figure 1(a)) with walking, rolling, and jumping modals for planetary exploration, which mimic the rolling capabilities of the Golden Wheel Spider as it escapes predators [7]. Barstow et al. designed and simulated an autonomous robotic exploration system (ARES) for planetary cave and lava tubes exploration (Figure 1(b)), which was inspired by red sea urchin's radial spines, frog tongue's whip-like motion, green gecko's foot, and orb-web spider's sensor in its legs [8]. Li et al. proposed a somersaulting soft robot, "SomBot", inspired by small stomatopod named *Nannosquilla decemspinosa* [9]. Using similar bionic principles, Patel et al. developed a dynamic bistable soft actuator using shape memory alloy and achieved multimodal soft robot locomotion, like crawling, swimming, and jumping [10]. Dylan et al. developed a pneumatic shape-change soft robot that adapts to environments better than an equivalent but non-morphing robot [11]. Gkliva used soft fluidic actuators to replace the rigid legs of RHex, enabling it to negotiate terrains of varying complexity [12, 13]. Similarly, Sadeghi developed a soft-legged wheel-based robot with terrestrial locomotion abilities [14]. Pneumatic actuators are widely used in the field of soft robotics. For instance, Ke et al. introduced a robotic system that employs stiffness preprogrammable soft pneumatic actuator, which showed superior kinetic, kinematic characterizations and sensing capabilities compared with the homogeneous one while coming across varying curvature objects [15]. Magnetic actuation has been applied in multimodal soft robots. This technique facilitates the creation of diverse configurations to achieve distinct motion patterns or capabilities [16]. In recent years, European Space Agency (ESA) has been looking for systems that would land on the lunar surface, identify and access a cave and contribute to the scientific exploration of the Moon [17]. NASA also proposed the "Moon Diver" mission with the "Axel" robot in order to return to Mare Tranquillitatis for collecting information on the chemistry, mineralogy, and morphology of these intact bedrock layers (Figure 1(c)) [18]. NASA's Jet Propulsion Laboratory designed a new Pop-Up Flat Folding Explorer Robot (PUFFER, Figure 1(d)) inspired by origami, which can fold flat to stow for launch and change shape according to the obstacles encountered [19]. For future planetary exploration, Kim et al. developed a cable-driven rolling robot, "Super Ball Bot" (Figure 1(e)) [20]. Naclerio et al. proposed a pneumatic steerable soft-growing robot that can navigate the underground environment (Figure 1(f)) [21]. Natural lava tubes on the Moon or Mars are the ideal candidates for scientific investigation, human habitation, and in situ resource utilization [22]. Increasing demand for robots can be expected for future space missions, including soft robots that are yet to be developed. Developing a lava tube exploration robot for unknown multi-terrain conditions is particularly of interest.

As mentioned above, modeling and simulation of soft robots are challenging, especially in the application and development of professional software. Commercially available software such as ABAQUS, ANSYS, and COMSOL have been involved in the soft robotics field [23], while they are primarily used in structural analysis in quasi-static conditions. In addition to direct theoretical modeling, like continuum mechanics models, geometrical models, and discrete material models [24], some researchers have also worked on developing soft robot simulation environments/tools. For instance. Hiller and Lipson developed the "VoxCAD" to simplify the modeling of robots with varying actuating materials and collisions [25]. Gazzola et al. developed "Elastica" to simulate the dynamics of soft filaments using the Cosserat rod theory [26]. Grazioso et al. presented a dynamic simulation environment, "SimSOFT," by combining the Finite element (FE) method, Cosserat rod theory, and screw theory, which can be helpful in the design, analysis and control of soft continuous robots [27]. FE modeling is employed to solve nonlinear deformation with prior knowledge of the material properties [28]. The open-source framework "SOFA" not only works for flexible continuum manipulators but also does a great job in soft robotic arms [29]. With the development of multi-flexible body dynamic techniques, RecurDyn can also be used for soft-body and rigid-flexible coupled robot simulation, especially in the dynamic analysis [30].

In summary, from the perspective of planetary lava tube cave detection, bionic design, and soft robot modeling and simulation, the main contributions of this study are as follows:

(a) A soft hexapod robot inspired by salamanders, inchworms, and cockroaches was designed and fabricated with multimodal characteristics for future planetary exploration, capable of walking, crawling, pronking, and rolling, as well as bionic combinations for obstacle crossing.

(b) A simulation framework and a rigid-flexible coupled finite element dynamics simulation model of the robot were

developed and justified through experiments, which have substantial application potential in optimization of the soft robot design, motion simulation of soft robots, and dynamic analysis with consideration of planetary environments.

(c) The proposed multimodal motion patterns were validated using an actual soft hexapod robot prototype, the untethered locomotion was achieved, and the experimental results demonstrated the potential of this robot for applications in diverse complex terrain environments.

The remainder of this paper is organized as follows. In Section 2, we demonstrate the soft hexapod robot prototype's bionic research objectives, design concept, and components. The procedure and theoretical modeling and simulation are presented in Section 3. Section 4 introduces the experimental setup and reports the experimental results. Finally, conclusions and discussions are presented in Section 5.

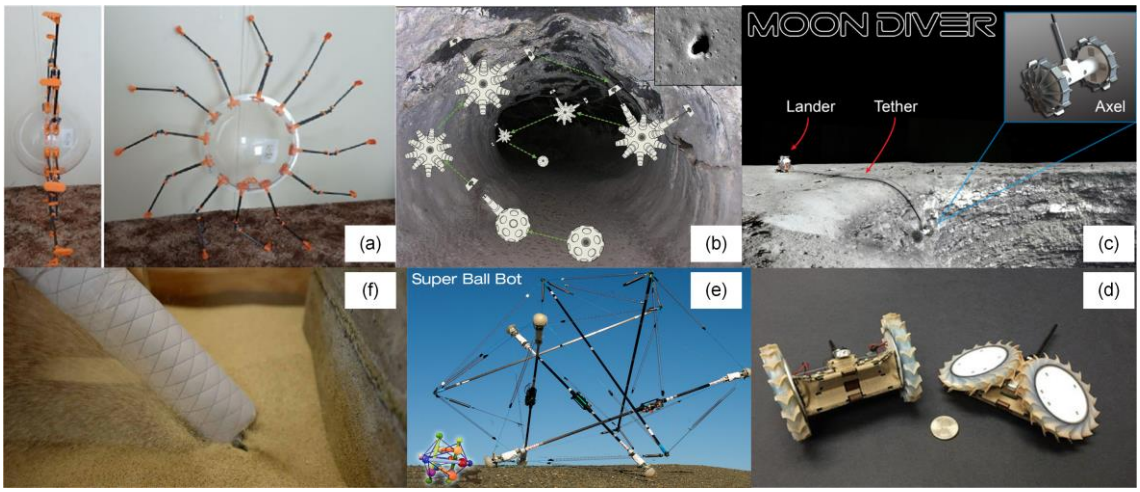

Figure 1 Robots for planetary exploration: (a) Spider Rolling Robot (SSR) [7], Copyright © 2023 Elsevier; (b) autonomous robotic exploration system (ARES) [8], Copyright © 2022 by the American Institute of Aeronautics and Astronautics (AIAA), Inc.; (c) concept for the "Moon Diver" mission [18], Copyright © 2019 IEEE; (d) Pop-Up Flat Folding Explorer Robot (PUFFER) [19], Copyright © 2020 Springer International Publishing; (e) "Super Ball Bot" [20], Copyright © 2015 NASA ; (f) soft-growing robot [21], Copyright © 2021 American Association for the Advancement of Science (AAAS).

2 Bio-inspired design and fabrication

2.1 Mission concept and bionic inspiration

Studies have shown that Mars and the Moon have many lava tube caves [22]. These interconnected lava tubes provide an underground network of paths which are of great interest for future scientific exploration and the construction of extraterrestrial bases. As shown in Figure 2, a lava tube is a hollow lava pipe formed when a lava flow cools and solidifies on the surface while the internal lava flow remains in high-temperature motion forward. Topographic features such as pits, pit chains, and skylights are often present on the surface of lava tubes. Skylights are openings at the top of caves or lava tubes that form round or oval, steeply pitted craters without edges. Most skylight entrances have a sizeable slope, with almost vertical inner walls and raised rocks. Although lava caves are ideal for humans to build bases to shelter from extreme temperature changes and harsh radiation, their stability is still questionable. The tubes have supposedly collapsed in some areas, leaving obvious deformations on the Moon's surface. It is assumed that sediments and scattered rocks may be present below the lava tube entrance and within the tubes [8]. Considering such a complex and rugged unknown terrain environment, we want to develop a flexible soft mobile robot with multiple motion functions with efficient movement capable of undertaking many different missions. That means, when there are rocks or other obstacles on the surface, the robot can walk or crawl over them. When encountering naturally formed hills or inclines, the robot can either climb them or use gravity to roll down freely while protecting the internal structure from any damage. Furthermore, during traversing a flat terrain, it can also choose to walk, run, or roll through faster, depending on the task requirements. In addition, the robot's compact size makes it easy to release via the mother rover and allows multiple robots to cluster for exploration.

The design of the robot proposed here draws inspiration from biological sources, primarily animals, such as the salamanders and inchworms. In the natural world, salamanders will produce a variety of defensive postures in the face of predator threats, such as curling the body to reveal the abdomen or arching the body to highlight the warning color (Figures 3(a) and (b)), some will also secrete skin venom, and some will break the tail to escape [31]. There is a species of terrestrial salamander (*Hydromantes Platycephalus*) in the Sierra Nevada Mountains of California that, when encountering a predator or when frightened, will quickly curl its body into a wheel shape and promptly roll down the slopes of rocky surfaces much faster than they can run on them (Figure 3(c)). This shape is achieved by bending the body laterally until the head is above the pelvis, the tail is curled ventrally, and the limbs are close to the body [32].

Another important biological organism, an inchworm, could use simple body bending to crawl above a rough substrate via alternating friction (Figure 3(e)), and many researchers have conducted extensive works in designing inchworm-inspired soft robots [33]. In addition, cockroaches can use their flexible limbs to traverse a variety of narrow gaps and rugged terrain. RHex is a cockroach-inspired, hexapod robot designed for locomotion in rough terrains (Figure 3(d)). It can drive over rocks, mud, sand, snow, and railroad tracks [13]. Inspired by the salamanders, inchworms, and cockroaches, a soft hexapod robot with multimodal motion named "SoSpider" is developed in this contribution. Differing from the majority of soft robots restricted to a single mode of motion, this innovatively designed robot can walk and run flexibly on complex grounds like a cockroach, roll down a slope like a salamander, pronk like a young deer, and crawl like an inchworm (Omega-arching locomotion). It can also achieve active rolling by utilizing the pushing action of its legs, like a golden wheel spider. Figure 2 also demonstrates the various locomotion styles of the proposed bio-inspired robot when it encounters different terrain environments. The robot can switch between different movement styles depending on the terrain, saving energy, and improving performance over obstacles as much as possible.

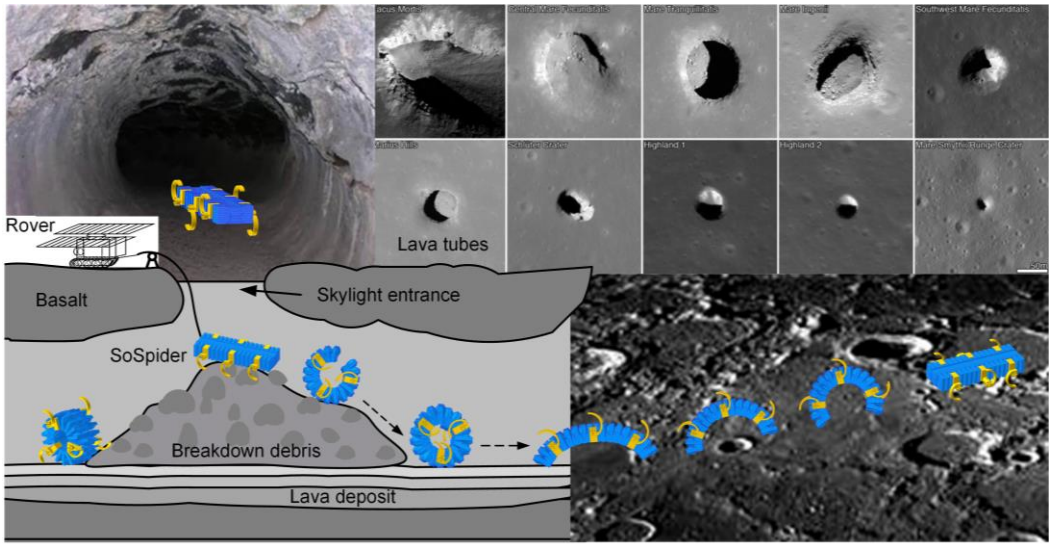

Figure 2 Lunar lava tube structures and bionic robot motion design concept, the background of lava tubes sourced from [34], Copyright © 2014 Elsevier.

Figure 3 (a) and (b) Antipredator posture of *Taricha rivularis* with forebody elevated [31], Copyright © 1977 American Society of Ichthyologists and Herpetologists (ASIH); (c) *hydromantes platycephalus* in the posture during rolling behavior [32], Copyright © 1995 Society for the Study of Amphibians and Reptiles; (d) a biologically inspired RHex robot [35], Copyright © 2016 IOP Publishing Ltd; (e) the inchworm crawling above branches [33], Copyright © 2022 American Association for the Advancement of Science (AAAS).

2.2 Bionic Locomotion Mechanisms

The proposed robot incorporates three fundamental motion modes: walking, rolling, and Omega-arching locomotion, drawing inspiration from various biological mechanisms. Walking is achieved by employing rotating joints that simulate the walking motion of cockroaches' legs. Additionally,

the pronk motion can be realized by simultaneously oscillating all six legs back and forth, interacting with the ground.

For the rolling mode, the robot's body is designed to curl up into a wheel-like shape similar to salamanders. To achieve this, a pneumatic network is employed, enabling the body to transform into a wheeled configuration. Rolling can be categorized into two cases: active rolling and passive rolling. Passive rolling utilizes the force of gravity on sloped terrain to achieve movement, while active rolling relies on the propulsion generated by the legs. Moreover, the curled wheeled structure provides protection for the internal electronic components and driving units of the robot.

The Omega-arching locomotion of inchworm consists of multiple motion segments, with only the first and last segment touching the ground, while the middle segment bends into an Omega shape and provides the driving force through its muscle contraction and extension to move it forward. The middle part of the inchworm does not touch the ground, and only realizes its movement by alternating the two ends of the head and tail. This motion can be achieved by the control of on-off switching of the curl up pneumatic body and adjusting the friction of the robot's front and rear feet.

2.3 Robot Design and Fabrication

The parts of the proposed soft mobile robot were designed using a computer aided design (CAD) software and were mainly fabricated from PLA plastic molds constructed with a 3D printer. The main structure of the robot body was inspired by pneumatic networks [36, 37] and the spine of living creatures. Figure 4(a) shows that the main soft body was divided into four parts during fabrication. Each part is molded in one piece using a silicone rubber (Dragon Skin 20, Smooth-On) and then bonded together with the same raw materials. The main curl module at the bottom achieves full body curl and head elevation when crossing the barriers. The fish spur-shaped design of both sides is for lateral bending and turning of the body. There are also separate air chambers underneath the turning module that are connected to the main curl module chambers through ventilation holes to serve as assistant curls. The servos to drive the walk and roll are placed in the slots position and are connected by long double-headed bolts through the limitation layer. Magnets are placed in the four corner chambers to aid shape retention after curling up.

The corresponding molds fabricated by a 3D printer are assembled, as shown in Figure 4(b). The definition and specific values of these chambers' dimensions are shown in Figure 5 and Table 1 separately. The design goals primarily involve minimizing actuating pressure and body mass while ensuring the structure maintains sufficient stiffness to resist damage or distortion caused by its own weight. These dimensional parameters were optimized values obtained by the RecurDyn simulation described in the next section which is verified by physical experiments. The overall size is designed with the reference to the lunar rover wheels, and the pneumatic unit is divided into 18 parts to strike a balance between reducing the angle of equal division and reducing the manufacturing difficulty. Additionally, the design experience in the literature is also very important for the determination of our design parameters [36, 38]:

(a) Thinner chamber walls generally lead to higher force output and require lower pressure for achieving maximum deformation;
(b) Increasing the chamber height tends to increase the force output while having minimal impact on the trajectory of the actuator tip;
(c) For fixed-length actuators, increasing the chamber height reduces the required pressure up to a certain threshold;
(d) Increasing the number of chambers also reduces the required pressure;
(e) Increasing the chamber wall thickness results in a higher required pressure.

The SoSpider has six 3D-printed semicircle legs, in which each leg is actuated by a single servo motor STS5420M (Feetech, Shenzhen) with a maximum torque of 25 kg·cm. We have designed the driving controller based on a single-chip microcomputer. The main control board is an integrated multi-functional custom printed circuit board (PCB) with microprogrammed control unit (MCU) of STM32F405, including servo motors (DC7.4 V) control, a mini pump (ZR370-03PM, DC12 V) and mini solenoid valves (DC12 V, Spike, Ningbo) control, pneumatic pressure sensors (WF100DP, 100 kPa), and an inertial measurement unit (IMU, BMI088). A lithium battery (7.4 V, 1500 mAh, 25C) is placed directly below the PCB. A wireless image transmission camera (5.8 G) is placed on the head of the robot for environmental exploration. By using pressure feedback and establishing the correlation between input pressure and the robot's body deformation angles, it becomes possible to determine the structural state of the robot. Additionally, the IMU sensor can be utilized to measure changes in acceleration, enabling the calculation of the robot's pose. The camera can provide real-time image transmission to an upper-level computer for environmental detection and future robot control. This allows the robot to select suitable motion modes based on its perception of the surroundings. The final prototype is shown in Figure 6. The overall mass of the prototype is 1.9 kg. The pneumatic solution is designed with a length of 306 mm, a width of 104 mm, a thickness of 48 mm for the flexible module part, and a maximum outer diameter of about 204 mm for the wheel shape formed after curling up (the outer diameter of the edge is about 186mm, the wheeled shape as shown in Figure 12(b)). The robot's C-shaped legs can be easily replaced with different radii or configurations. The height of the C-shaped leg shown in the figure is 50 mm, and the leg width is 12 mm. Besides, we stick sandpapers to increase

the friction on the bottom of the foot.

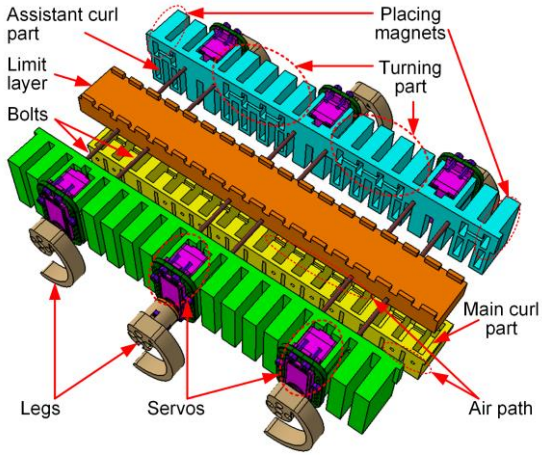

(a)

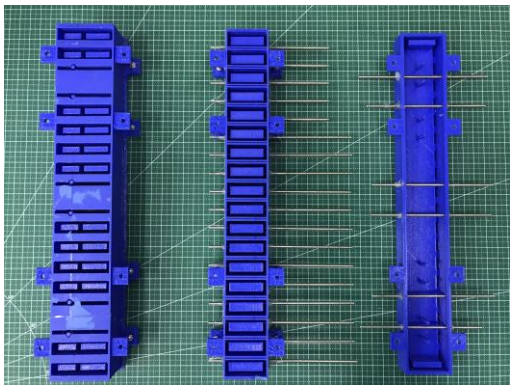

(b)

Figure 4 (a) 3-D model of the soft hexapod robot design; (b) 3D-printed molds for the silicone pneumatic networks.

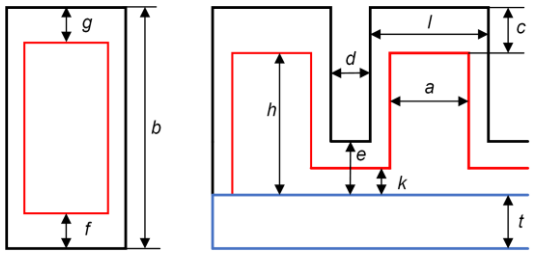

(a) (b)

Figure 5 (a) Top view of a single pneumatic network cross section; (b) front cross-sectional view the chambers. The symbols in (a) and (b) are descripted in Table 1

Table 1 Main structural dimensions of pneumatic networks (Units: mm)

Description	Symbols	Main curl part	Assistant curl part	Turning part
Inside length of the air chamber	*a*	8	5	5
Wide of a single network	*b*	36	37	23
Thickness of the top wall	*c*	4	4	4
Gap between adjacent chamber	*d*	3	6	6
Thickness of the connection part	*e*	5	5	5
Thickness of the inside lateral wall	*f*	3	3	4
Thickness of the outside lateral wall	*g*	3	4	4
Height of the air chamber	*h*	25	21	30
Height and width of the air path	*k*	3	3	3
Outside length of the air chamber	*l*	14	11	11
Thickness of limit layer	*t*	15	—	36

2.4 Robot legs control

A PID controller was used in the servo motors' position control. Tripod gait is the most commonly used in hexapod robots, in which legs' arrangement is divided into two groups, where {1, 4, 5} are the first group, {2, 3, 6} are the second group with different phases. Here the odd numbers are on the left side of the body, and even numbers are on the right side (as shown in Figure 6). The legs' phases typically divide into off-ground and ground contact phases correspond to fast and slow phases during hard ground locomotion. As shown in Figures 7(a) and (b), the fast and slow phases are implicitly defined by the triplet $\{\theta_s, \theta_0, d_f\}$, where θ_s is the angular extent of the slow phase, θ_0 is the angular location of the center of the slow phase, and $d_f = t_s / t_c$ is the duty factor of the slow phase. Then the control vector for a single leg can be written as $u = \{\theta_s, \theta_0, t_c, t_s\}$. For instance, if at the initial moment, all the legs are positioned at 180°. When the control vector is set to {60°, 30°, 3 s, 1.2 s} for the tripod gait, Figure 8(a) illustrates the angle variation of each leg over time based on the feedback received from the servo motors. The controller for turning in place employs the same leg profiles as for running except that the contralateral set of legs rotates in opposite directions. Turning during forward locomotion can be achieved by using different perturbations as the control vector $u_l = \{\theta_s, \theta_0 + \Delta\theta_0, t_c, t_s + \Delta t_s\}$, and $u_r = \{\theta_s, \theta_0 - \Delta\theta_0, t_c, t_s - \Delta t_s\}$ for the legs on the left and right side, respectively. Besides, turning locomotion can also be easily achieved using the pneumatic turning part.

An open loop pronk is an uncommon single-beat gait where all six feet leave the ground and land at the same time, which is inspired by young deer and springbok for its habit of repeatedly leaping high into the air when startled [39]. The controller switches between two control actions periodically as a function of the clock state, as shown in Figures 7(c) and (d). Furthermore, the motion cycle of the six legs remains consistent, with a repetitive swinging motion from front to back. When the control vector is set to {60°, − 30°, 3 s, 1.2 s} for the pronk gait, Figure 8(b) illustrates the angle variation of each leg over time based on the feedback received from the servo motors. It should be noted that the direction of rotation of the servos on both sides of the robot is opposite during actual control.

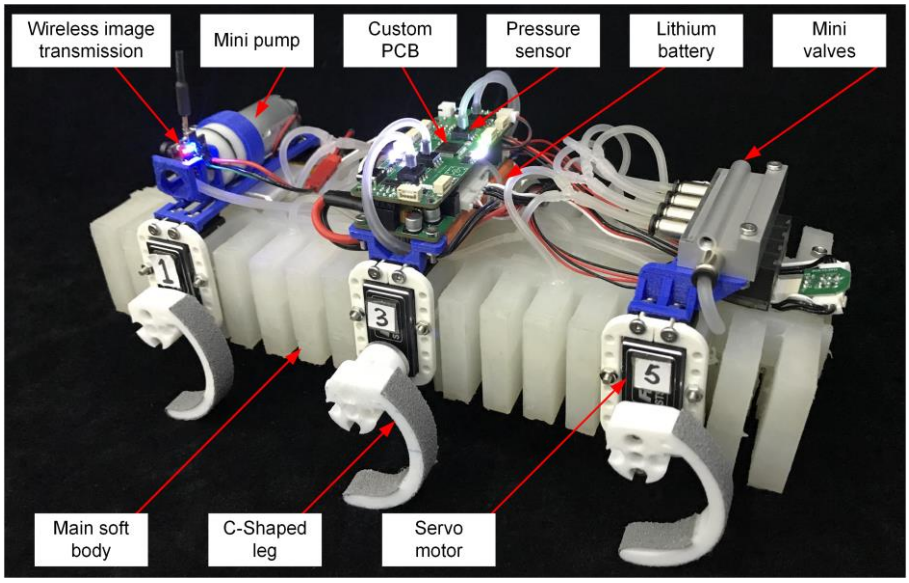

Figure 6 Prototype of the SoSpider

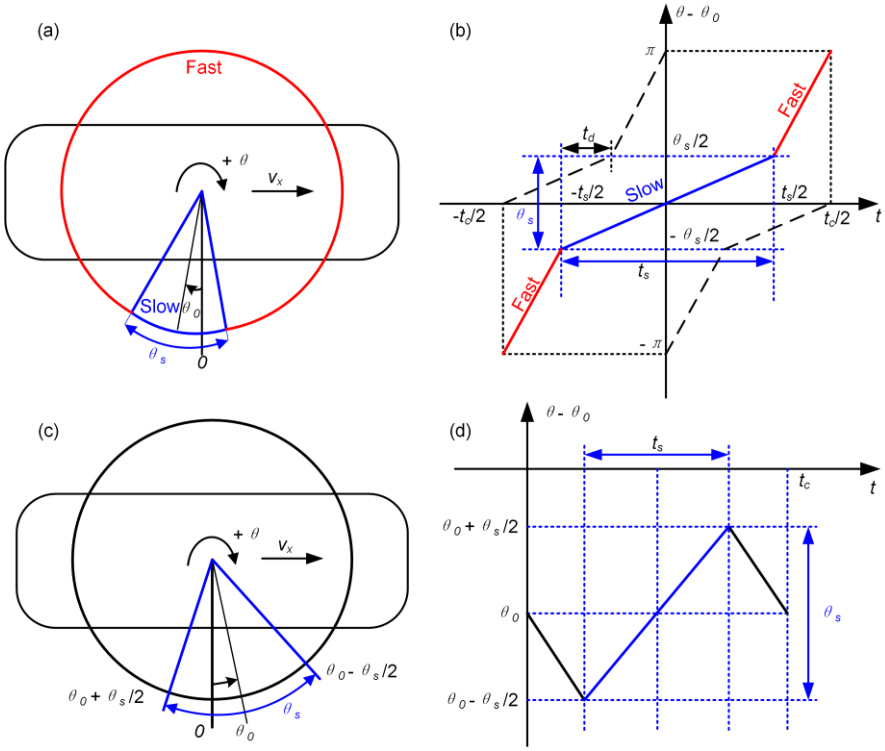

Figure 7 (a) Each leg is composed of a fast phase (red) and a slow phase (blue) in the tripod gait, θ_s and θ_0 (leg angle offset with respect to the vertical) define the angular extent and center of slow phase; (b) leg angle θ as a function of time t during one period t_c, t_s is the duty of the slow phase, t_d is the duration of all six legs are contact with the ground, the phase of the other tripod is shifted by $t_c/2$; (c) each leg oscillating in the same phase of the pronk gait, where θ_0 is the center of the sweep angle θ_s; (d) leg position profile as a function of time t in pronk gait, where t_c is the gait period, and t_s is the time from aerial to touchdown.

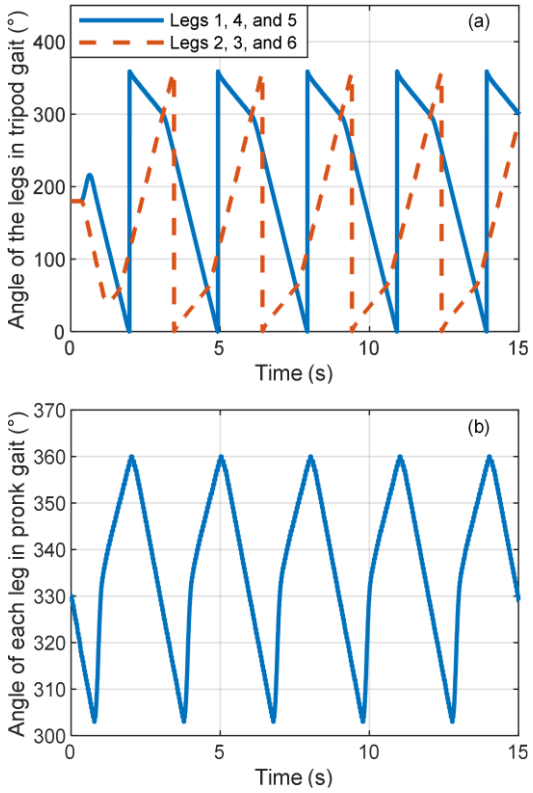

Figure 8 (a) The angle variation of each leg over time for the tripod gait; (b) the angle variation of each leg over time for the pronk gait.

3 Modeling and simulation

3.1 Simulation framework

Unlike rigid robots driven mainly by electrical motors or hydraulic actuators, soft robots have various actuation methods, including but not limited to pneumatic, cable-driven, and intelligent materials like shape memory alloys. Although the actuation principle is complex, it can be simplified using distributed pressure, equivalent springs, equivalent forces, or moments [30]. For soft robots or rigid-flexible coupled robots, we have developed a set of corresponding dynamics modeling and simulation processes, the details of which are shown in Figure 9. The simulation was conducted in the RecurDyn software with an import 3D model designed for the simplified prototype. In our case, the upper drive part is not considered, and the servos and legs are kept in line with the prototype's weight by giving the corresponding density. The soft silicone body is meshed with hexahedral elements and a hyperelastic material model is assigned. Hexahedral elements are used as they can better resemble the hyperelastic stress-strain relationship under large deformations. In addition to constraints and rotating joints, the definition of hyperelastic material properties and contacts is the most critical and is described in the next section.

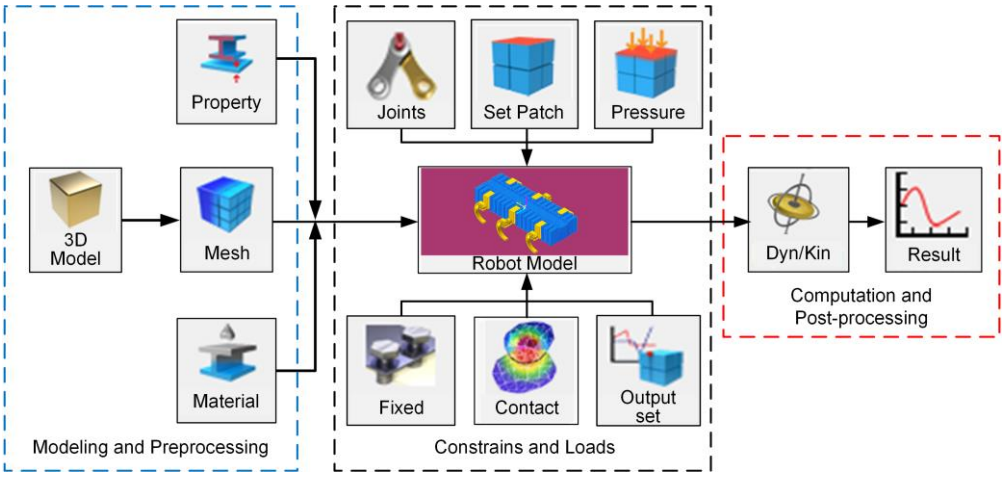

Figure 9 Dynamic Finite Element (FE) modeling and simulation framework for the soft robots.

3.2 Hyperelastic constitutive model

To develop a simulation of a soft robot, it is first necessary to determine its material parameters. The properties of rigid materials can be easily obtained by consulting manuals or existing material libraries. However, material parameters of soft materials, especially silicone of different hardness, need to be obtained through experiments. Although the relevant literature has reported many experimental works [40], a more reliable way is to conduct experiments again to determine the material parameters, as there may be differences in the manufacturing process and environment of materials. Due to the nonlinear relationship between stress and strain of the soft silicone polymer, its properties are described by a hyperelastic constitutive model. Among the constitutive models for hyperelastic materials, the Ogden model can provide a more accurate description than the neo-Hookean model or the Mooney-Rivlin model, especially at large deformations [41]. The expression of the Ogden model is as follows:

$$U = \sum_{i=1}^{N} \frac{\mu_i}{\alpha_i} (\lambda_1^{\alpha_i} + \lambda_2^{\alpha_i} + \lambda_3^{\alpha_i} - 3) \quad (1)$$

where μ_i and α_i are empirical material constants, N is the number of terms, λ_i is principal stretches. Besides, the silicone material's Young's Modulus (E) can be obtained as follows:

$$G = \frac{1}{2}\sum_{i=1}^{N}\mu_i\alpha_i \tag{2}$$

$$E = 2(1+\nu)G \tag{3}$$

where G is the shear modulus, E is the Young's Modulus, and ν is the Poisson's ratio.

For the Dragon Skin 20 soft silicone material, the Ogden model parameters were obtained based on a nonlinear least-squares method and Levenberg-Marquardt algorithm [40] by fitting the data obtained from uniaxial stretching experiments. The results of tensile tests and data fitting are shown in Figure 10. The fitted coefficients are as follows: $\mu_1 = -0.6830$, $\mu_2 = 0.8864$, $\mu_3 = -0.1750$, $\alpha_1 = 5.1017$, $\alpha_2 = 5.1673$ $\alpha_3 = 5.4285$, all the μ terms have units of MPa while all the α terms are dimensionless. In addition, the shear modulus (G) of the material can be obtained as 72.8 kPa, the Young's Modulus (E) can be obtained as 218.4 kPa from Equations (2) and (3), with a Poisson's ratio of 0.5 for incompressible material. The Young's modulus can be further used to calculate the contact parameters as shown in the following section.

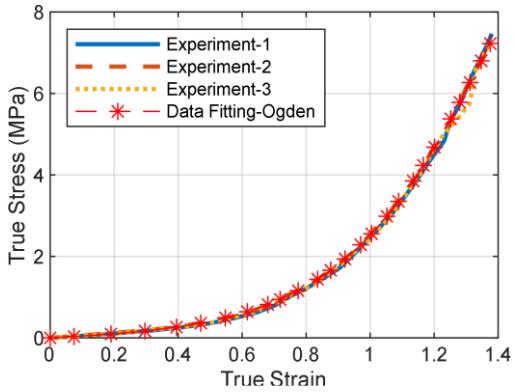

Figure 10 The uniaxial tension test results and data fitting curves.

3.3 Contact model

The simulation model involves many contacts, including the foot-terrain interaction, contacts between each pair of pneumatic networks, and contacts between the soft body and ground. The setting of the contact model and contact parameters is crucial to the success of the simulation. The "Geo Surface Contact" in RecurDyn software was selected to represent the interaction mechanics as it is suitable for the analysis of flexible bodies and has a higher computational efficiency. A "Geo Surface Contact" is a General Geometry Contact which can analyze the contact between any kinds of geometries. The geometry can be a rigid body or a flexible body and they can have any kind of shapes. While, its basic contact mechanism is still based on Hertz contact model. The contact model is generally divided into two parts: the model in the normal direction and the model in the tangential direction [42, 43]. The normal force is calculated as follows:

$$F_N = k\delta^{m_1} + c\frac{\dot{\delta}}{|\dot{\delta}|}|\dot{\delta}|^{m_2}\delta^{m_3} \tag{4}$$

where k and c are the stiffness and damping coefficients, respectively. δ and $\dot{\delta}$ are a penetration parameter and its time differentiation, respectively. m_1, m_2, and m_3 are the stiffness, damping and indentation exponents, respectively. The stiffness coefficient that is based on the Hertz contact theory [44] is calculated using the following equations:

$$k = \sqrt{\frac{16RE_k^2}{9}} \tag{5}$$

$$R = \frac{R_1R_2}{R_1+R_2} \tag{6}$$

$$E_k = \frac{E_1E_2}{E_2(1-\nu_1^2)+E_1(1-\nu_2^2)} \tag{7}$$

where R is an equivalent contact radius, R_1 and R_2 are the contact radii of the contact pair, E_k is an equivalent Young's Modulus, E_1 and E_2 are Young's Modulus of the materials in contact, and ν_1 and ν_2 are Poisson's Ratios. These parameters can be used to solve for contact stiffness and apply it in practice to robot simulation.

The friction force is determined as follows [45]:

$$F_T = \mu(v)|F_N| \tag{8}$$

where F_T is the friction force, $\mu(v)$ represents friction coefficient that is determined by the tangential relative velocity (v) on the contact point, and F_N is the normal contact force.

4 Experimental and Simulation Results

4.1 Basic deformation analysis

The turning and curling parts are modeled separately to simplify the model. The maximum mesh element size is 5 mm, the minimum element size is 0.75 mm, the number of elements of the turning part is 31,887, and the number of elements of the curling part is 37,078. Equations. (5)-(7) are used to calculate the stiffness coefficient and the radius of the contact pair was usually set as $R_1 = R_2 = 5 \times 10^5$ mm for the face-to-face contact. The rigid surface of the servo motor is aluminum material with Young's Modulus of 70 GPa, and Poisson's ratio of 0.32. The stiffness coefficient is 97 N/mm between the silicone and silicone (Dragon skin 20), and 194 N/mm between the silicone and the rigid surface. Besides, the numerical value of damping coefficient is usually set as $c = k/10^4$ based on experience. The stiffness,

damping and indentation exponents are set to their default values, with $m_1 = 2$, $m_2 = 1$, and $m_3 = 2$. Friction between pneumatic networks is not considered, hence the friction coefficient is set to 0.

As shown in Figures 11(a) and (b), the simulation model and prototype can turn up to 60°. The relationship between the input pressure and output turning angle is shown in Figure 13(a). The curl-up simulation model and prototype can also reach the design goal as they can curl up to a wheeled shape under 55 kPa. The snapshots of the curl-up simulation and experiment are shown in Figure 12. The simulation can reproduce the prototype's deformation process, and the relationship between the curl deformations' input pressure and output bending angle of the half curl-up part is shown in Figure 13(b). From the experimental results, as shown in Figure 13, we can find a significant difference in the deformation of the module during inflation and deflation, mainly due to the viscoelasticity and the Mullins effect of the soft silicone material. In the turning part, the mean relative error between the simulation results and the experimental average values is 26.98%. In the curl-up deformation, the mean relative error is 14.59%. It is important to note that the zero values at the beginning were not included in the error calculation. The sources of error can be attributed to two factors. On the one hand, errors may arise from simplifying the model and inaccuracies in simulating materials or contact parameters. On the other hand, errors can occur due to the measurement of experimental data. In the turning component, the larger error can be attributed to the increased gap between adjacent chambers and the presence of a servo motor in the middle of the turning part.

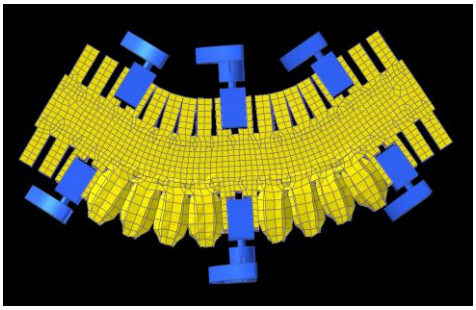

(a)

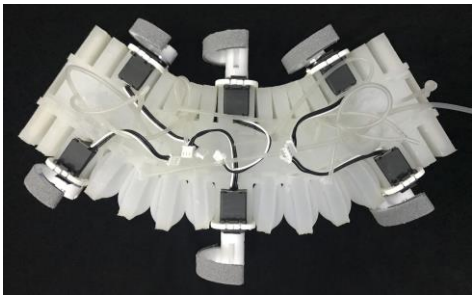

(b)

Figure 11 (a) The snapshot of simulation results of the turning part undergoing inflation at a pressure of 80kPa; (b) the experimental result snapshot of the turn part undergoing inflation at a pressure of 80kPa.

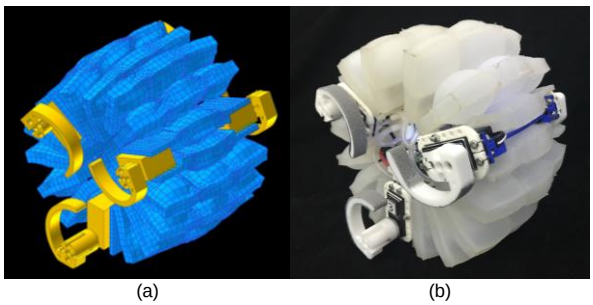

(a) (b)

Figure 12 (a) The snapshot of simulation results of the curl-up part undergoing inflation at a pressure of 55 kPa; (b) the experimental result snapshot of the curl-up part undergoing inflation at a pressure of 55 kPa.

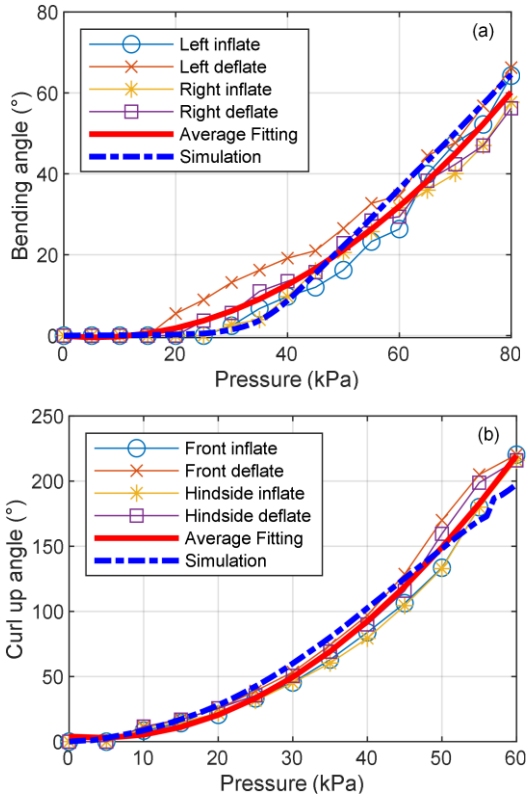

Figure 13 (a) The relationship between the air pressure of the turning part and the bending angle; (b) the relationship between the input air pressure and the curl up angle of the half curl-up part.

For future robot analysis and control, we fitted the average value of the experimental results and obtained the formulas for the air pressure and deformation angle, as shown below.

$$\Phi_{\text{Turn}} = 0.01094P^2 - 0.1219P - 0.09508 \quad (9)$$

$$\Phi_{\text{Curl}} = 0.06917P^2 - 0.5548P + 3.96 \quad (10)$$

where Φ_{Turn} and Φ_{Curl} are the bending angle of the turning part and curl-up part, respectively, and P represents the input pressure.

4.2 Pronk under lower gravity

Simulation studies are particularly valuable in scenarios

where experimental testing is not feasible, such as simulating outer space environments like the extraterrestrial conditions. Due to the robot's mass and servo power limitations, it is currently difficult to achieve fast pronk in the Earth's gravity environment. The experimental results with the control parameters as $\theta_0 = -30°$, $\theta_s = 60°$, $t_c = 0.5$ s, and $t_s = 0.2$ s are depicted in Figure 14, the pronk gait can achieve forward movement but cannot achieve obvious jumping. However, the gravity of extraterrestrial environments differs from that of the Earth, and space systems often require significant financial and human resources to conduct low-gravity experiments. Simulation can effectively reduce the cost of analyses. The low gravity environment also facilitates the movement of the robot to overcome gravity and save energy on the one hand. The gravity on the Moon, Mars, and the Earth are known to be $G_{Moon} = 1.6$ m/s², $G_{Mars} = 3.7$ m/s², and $G_{Earth} = 9.8$ m/s², respectively. Here we simulate the pronk locomotion under the Moon and the Mars gravity with the same control parameters. Besides, here we used legs with a diameter of 60 mm and 5/8 wheeled shape to increase the touchdown area and avoid overturning. Moreover, a pressure of 10 kPa was acted on the curl part to promote the stiffness of the soft robot body. The snapshots of simulation results under the Moon gravity environment are shown in Figure 15. Figure 16 illustrates the displacement of the body's center of mass in horizontal and vertical directions. It can be seen that the low gravity environment helps to improve the robot's motion efficiency and reduce the fluctuation of the body.

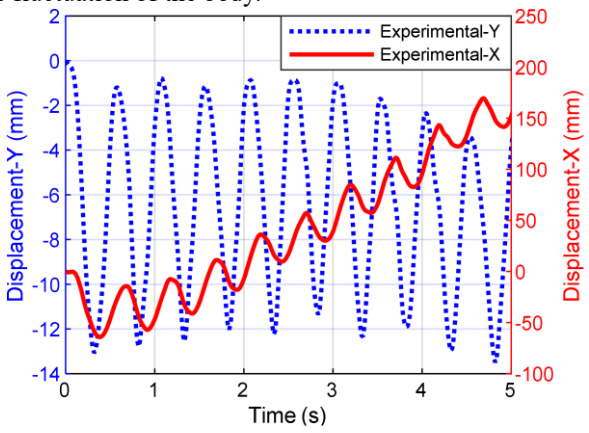

Figure 14 Experimental results of the robot's displacements under Earth's gravity condition using the pronk gait.

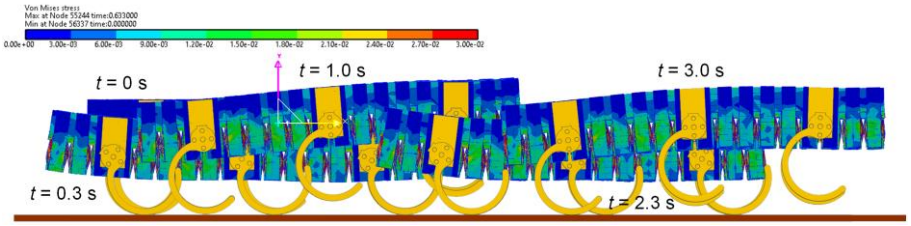

Figure 15 Simulation snapshots of pronk gait locomotion under the Moon gravity condition.

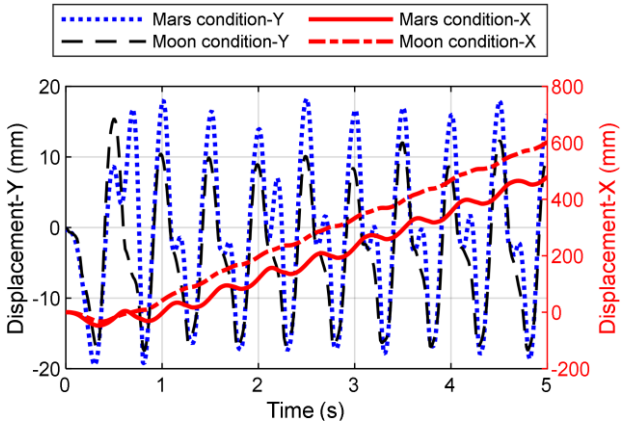

Figure 16 Simulation results of the displacements in horizontal and vertical directions under the Mars and Moon gravity conditions.

4.3 Rolling performances

Rolling motion is ideal for rapid movement over flat terrain and rapid descent from slopes using gravitational potential energy, saving energy and protecting internal electronics. The experiment with free rolling is shown in Figure 17 with a slope of 12.7°. This slope is set up using a stationary treadmill. The robot's main body is made of silicone material, and 18 pneumatic units after curling only approximate wheel shape. Due to not being infinitely close to a cylindrical shape and the presence of soft material deformation, when the slope of this testbed is less than 12°, the robot will still be stationary on the slope after curling but can roll down after being disturbed. When the slope is greater than 12°, the robot can overcome resistance to roll down under the action of its gravitational potential energy, like the salamanders roll down from the hill, as shown in Figure 3(c). In this paper, we used Kinovea (Version 0.9.5, Charmant, J. et al. https://www.kinovea.org) software to process the motion videos, where we can get the displacement, velocity, and acceleration of the marker point through the motion video. Figure 17 also shows the motion trajectory and acceleration of the marker point on a servo at the critical moment. More details of the passive rolling motion can be found in the Supplementary Video S1.

The SoSpider can be rolled down passively on slopes by gravity. While on a flat terrain, it can also be driven by the C-shaped feet to roll the body. As shown in Figure 18, we increased the height of the leg structure to 65 mm to increase its force arm to push the robot to roll. Accordingly, the width of the entire prototype has also changed, and the front and back staggered distribution to avoid interference

between the legs. The widest point of the entire machine is 211 mm. In this experiment, the inflation time is 48 s, and the six legs are divided into three groups, the front {1, 2}, middle {3, 4}, and back {5, 6}: the left and right sides are driven simultaneously. Each group of legs rotate from 180° to 0°, touches the ground, and then quickly recovers 180° again. The swing interval is 0.8s. Through several experiments, the robot can roll 1 ~ 1.5 revolutions under this drive condition, which is also related to the battery level, as the magnitude of the servo torque depends on the voltage. In Figure 18, the robot is in an Omega shape after deflating at the rolling end, and the marked point's horizontal relative displacement is about 890 mm. The instantaneous rate of the marked point shown in the figure is up to 0.74 m/s, and detailed actions are shown in Supplementary Video S2. Currently, the robot is open-loop controlled and can stop rolling by interaction with the ground in a flat terrain. After the robot is stopped, in one case, it is in the same pose as in the initial case; and in another case, it is in the Omega shape as shown in the figure; even so, the robot can continue its travel by changing its motion pattern, as shown in Section 4.4.

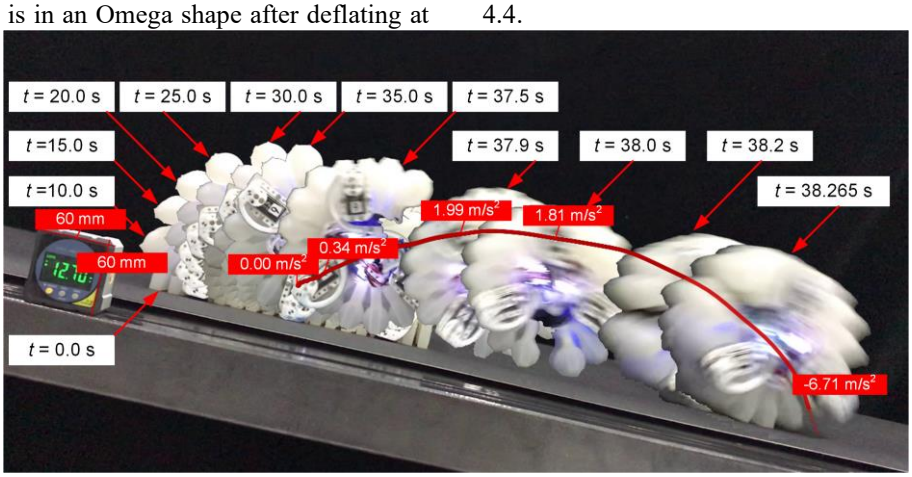

Figure 17 SoSpider passive rolling down from the slope, the red line shows the trajectory of the marked point on the middle servo, and the marked value is the instantaneous acceleration.

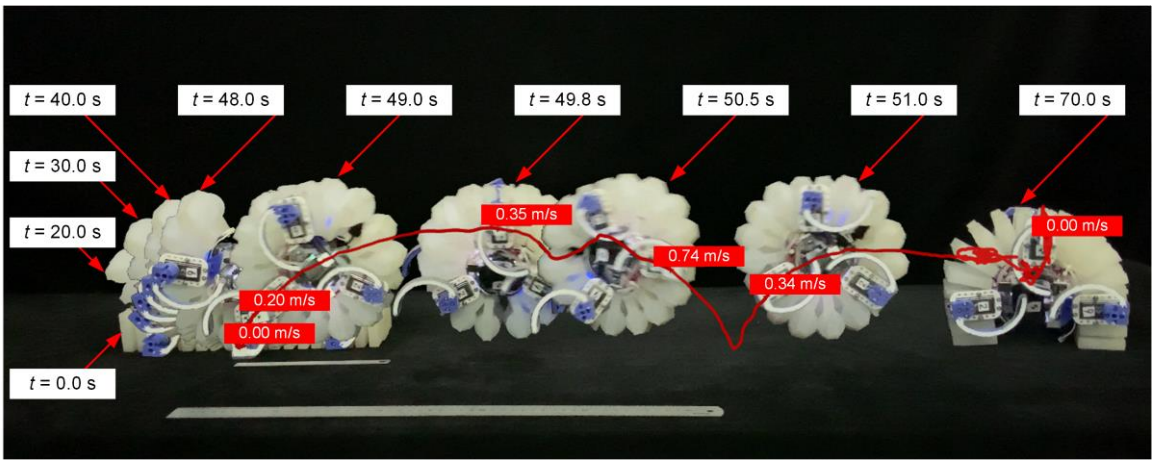

Figure 18 Snapshots of active rolling motion experiment, the red line shows the point trajectory of the middle servo's rotation axis with instantaneous velocity of the marked point.

4.4 Omega-arching locomotion

The Omega-arching locomotion is achieved using different friction strategies between the front and the rear feet. Since the robot body is a symmetrical structure, its creep direction is determined by the arrangement of the legs. Here we designed a pair of feet with different structures and frictions for creeping forward, as the inchworm shown in Figure 3 (e). The front end of the forefoot is inclined at 60°, and the rear end of the hind foot is inclined at 70°. We increase the friction on the bottom of the foot by applying silicone pads at different locations. In addition, the bottom part of the circuit board also added a protective shell. When inflation begins, the bottom surfaces of the front and rear feet make contact with the ground. The friction between the bottom surface of the front foot and the ground is greater than that of the rear foot. As a result, the front foot anchors while the rear foot slides forward. Once the body reaches a certain shape after inflation, both the front and rear feet gradually transition to make contact with the ground on their respective sides. At this point, the inflation is stopped, and the deflation process begins. Due to the higher friction at the

side of the rear foot compared to the front foot, the rear foot anchors during deflation while the front foot moves forward. This continues until the gas is completely expelled, completing one crawling motion. This process repeats cyclically, enabling continuous movement.

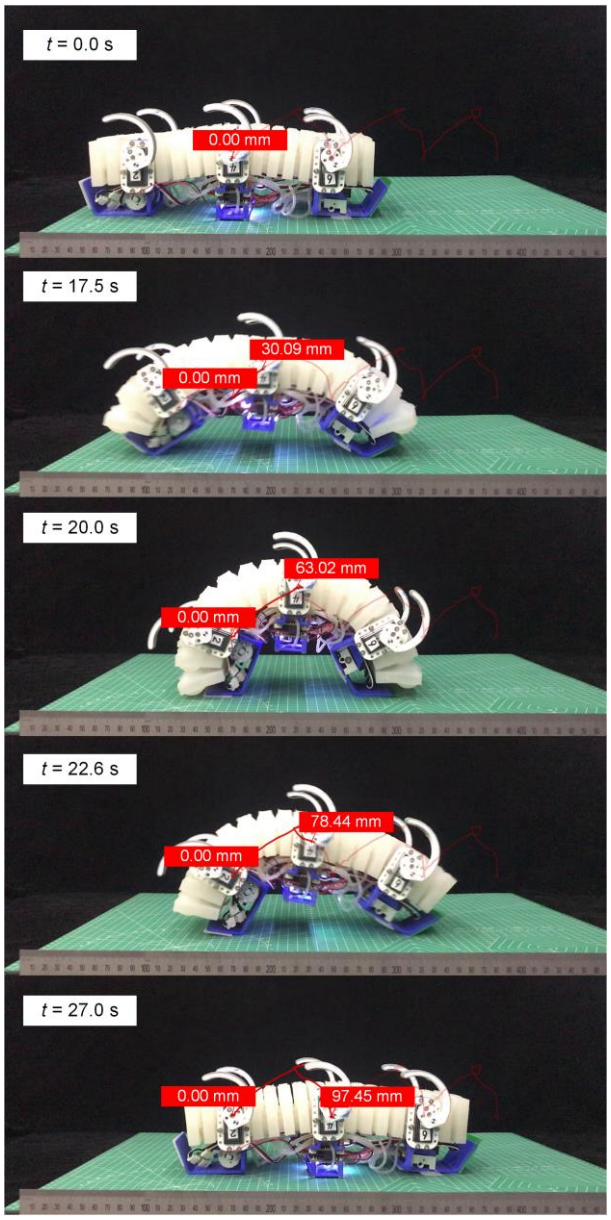

Figure 19 Snapshots of the Omega-arching locomotion in one period, where the red line indicates the trajectory of the marked point, and the marked value is the instantaneous displacement.

The period for the Omega locomotion was set as 20 s for inflation and 7 s for deflation. The maximal input pressure in one cycle is about 50 kPa. The experimental snapshots are shown in Figure 19, and the horizontal relative displacement results are shown in Figure 20. The average displacement in one period is 70 mm, and the maximum value can reach 97 mm in one cycle movement. A locomotion video can be found in Supplementary Video S3. Although the movement speed of this mode is limited, the Omega-arching locomotion can be employed as an alternative mode of movement, especially in situations where there is a failure in the legs or motors. This type of locomotion allows the robot to continue moving forward, significantly enhancing the overall reliability of its mobility, especially in unknown space exploration environments.

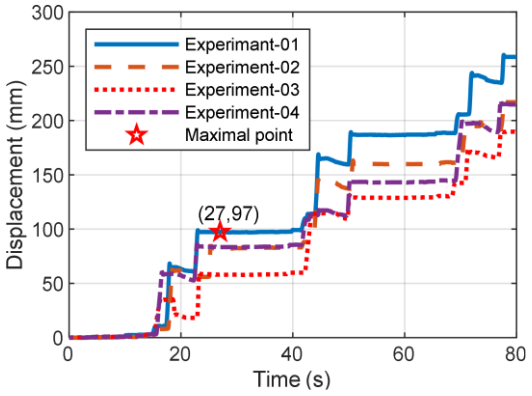

Figure 20 The horizontal relative displacement results versus times in Omega-arching locomotion experiments.

4.5 Adaptability experiments

The control vector $\{\theta_s, \theta_0, t_c, t_s\}$ for the wheeled leg with variable speed motion is set to {60°, 30°, 3 s, 1.2 s} according to the control strategy as shown in Figures 7(a)–(b) and Figure 8. In addition to the most commonly used tripod gait, the robot can also use a synchronized gait in which all six legs move simultaneously without phase differences. As the lava tube floors have congested pathways, cracks, and slopes, it is necessary to test the traversal capability of the robot gaits. In addition to rolling down from a slope and locomotion on level ground, the proposed robots can also adapt to some other environments, such as crawling up to the slope, turning during the forward locomotion, and navigating rocky and obstacle terrain (recorded in the Supplementary Videos S4-S7).

Currently, the robot can crawl up to a slope of 35° using a tripod gait or synchronized rotation gait (shown in Figure 21(a)). When using the lower height C-shaped legs (50 mm), the robot can also climb slopes up to 37.5° due to the lowered center of mass. Figure 21(b) shows the robot crawling up to the slope of 37.5° using a tripod gait. The robot can also realize the turning during the forward locomotion by using the inflatable bending deformation of the bionic spine, as shown in Figures 21(c) and (d) for the left and right turns under the triangular gait, respectively. Climbing and turning are recorded in Supplementary Videos S4 and S5, respectively.

Various movement patterns can be generated by combining C-shaped legs and a soft pneumatic body. When the leg height is lower than the obstacle, the body is easily blocked by the obstacle. Here by using the bionic soft pneumatic body and inflating the front half to raise the head, the robot

can get through the obstacle with a height of 70 mm (see Figure 21(e) and Supplementary Video S6). For debris and rock steps that may be encountered in the lava tube terrain of Mars or the Moon, we used Martian rubble substitutes and rock slabs to simulate lava tube step terrain and test the adaptive performance of the robot. Figures 21(f)–(h) show the snapshots of test results. The robot can easily navigate gravel and rocky terrain and roll down slate slopes. Details can be found in Supplementary Video S7.

In Table 2, a comprehensive comparison is presented between SoSpider and other robots inspired by organisms in nature or designed for space exploration. Where BL/s means body lengths per second in Table 2. For length-scale reference, the robot is 100 mm by 150 mm when flattened, and 70 mm diameter by 150 mm when rounded, for the shape-change soft robot [11]. The length dimensions of the 3D printed frame for the bistable soft actuator is 51.75 mm [10]. SoSpider stands out by accomplishing not only basic movement functions like walking, crawling, and rolling but also by being capable of untethered movement without the need for additional wire or tube ties. Moreover, this untethered design, coupled with its diverse range of motion modes, enhances the reliability of the robot's movement and enables it to explore a wide variety of environments. Consequently, SoSpider exhibits great potential for planetary exploration.

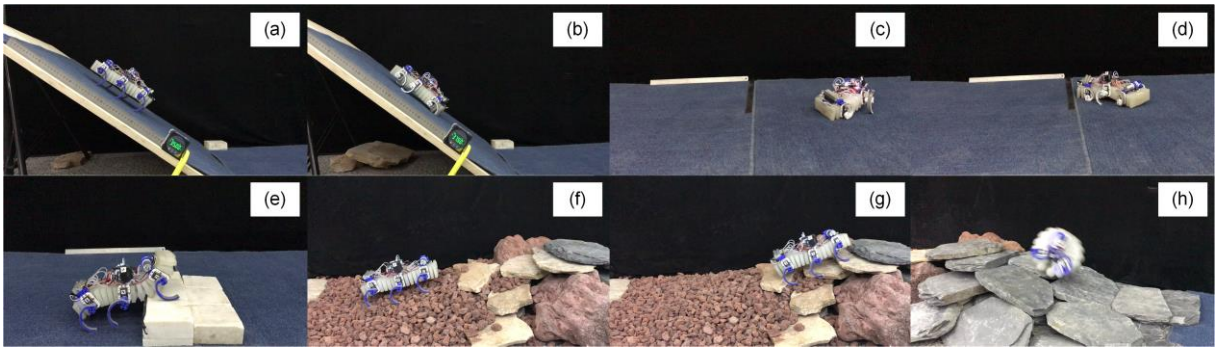

Figure 21 (a) Climbing 35° slopes using synchronized rotation gait;(b) climbing 37.5° slopes using a tripod gait; (c) right side inflation for the left turn of tripod gait; (d) left side inflation for the right turn of tripod gait; (e) front inflatable to achieve 70 mm height over the barrier; (f) walking on the rubble slope; (g) climbing up the stone steps; (h) rolling down the slope of the slab.

Table 2 Comparison with related robots

Robots	Walking / Running	Rolling / Wheeled	Crawling / Worming	Pronking / Jumping	Untethered locomotion
SoSpider (Our robot)	√ >0.1 m/s	√ >0.7 m/s	√ >0.003 m/s	√ >0.03 m/s	√
GoQbot [6]	×	√ >0.5 m/s	√	×	×
SSR [7]	√	√	×	√	√
ARES [8]	×	√	×	√	√
SomBot [9]	×	√ 0.948 m/s	×	×	×
Robot using bistable soft actuator [10]	√ 0.07 BL/s	√ 1.33 BL/s	√ 0.08 BL/s	√	×
Shape-change soft robot [11]	×	√ 0.05 BL/s	√ 0.01 BL/s	×	×
RHex [13]	√ 0.55 m/s	×	×	√ 0.974 m/s [46]	√
Soft-legged wheel-based robot [14]	×	√ 0.209 m/s	√ 0.038 m/s	×	√
Axel [18]	×	√ 0.1 m/s	×	×	×
PUFFER [19]	×	√	×	×	√
Super Ball Bot [20]	×	√	×	×	√
Soft-growing robot [21]	×	×	√ 4.8 m/s	×	×

5 Conclusions and discussions

This work designed and fabricated a bio-inspired multimodal soft pneumatic hexapod robot named SoSpider using silicone pneumatic networks and servo motors driven C-shaped legs for future planetary lava tube exploration. A rigid-flexible coupling FE dynamic simulation model was established for the soft hexapod prototype. The main soft body's fundamental bending and curl-up deformation was tested in simulation and experiments. The results have shown good agreement, justifying the design concept. The pronk gait was realized in dynamic simulation with simu-

lated low gravity environments on the Moon and Mars. Other locomotion types, including passive or active rolling, inchworm-like Omega-arching, and walking and turning on different barrier conditions, were all demonstrated in the untethered experiments. The robot not only has a wealth of movement modalities but also demonstrated robust obstacle-crossing performance, climbing a 37.5° slope, walking over 70 mm high obstacles, and navigating gravel terrains. Our robot prototype, especially its design and development process, can provide a reference for the innovative design of bionic robots. Our simulation framework also plays a crucial role in optimizing the design and conducting dynamic simulations for robots intended for extraterrestrial planet exploration.

Although some of the robot's performance could have been further optimized, all the intended design goals were achieved. The robot's bionic motion potentials are to be further explored. The proposed robot and simulation framework can potentially be applied in planetary explorations. However, there are limitations and possible alternatives. First, about the materials, we have not considered the extreme environment in outer space, like various radiation, high-energy particles, and extreme temperatures that could cause structural performance degradation or failure. More interdisciplinary research can be conducted in the future. Second, pneumatic actuation has certain application limitations in a vacuum environment like lunar, but it can be solved by carrying compressed gas cylinders or by chemical reactions to generate driving pressure. In addition, other actuation methods, such as cable-driven or shape memory alloys, can be used to achieve the same deformation. Third, FE simulation can help reduce experimental costs effectively. However, the computational time required for the simulation is of concern, which primarily depends on the performance of the Central Processing Unit (CPU) and the number of soft elements in the simulation. There is still a possibility of optimization in this area.

In future research, we will focus on optimizing the internal structure of the robot by fully enclosing the crawling foot within the curled body. We also plan to integrate all power and actuation components inside the soft body, using a flexible control board with soft sensors for a more integrated prototype. Furthermore, closed-loop and states transition control will be a research focus to enhance the intelligence of the robot.

Availability of data and materials

The datasets used and/or analysed during the current study are available from the corresponding author on reasonable request.

Supplementary Material

Supplementary Video S1: Passive rolling down from the slope.

Supplementary Video S2: Active rolling on a flat surface.

Supplementary Video S3: Omega-arching locomotion on a flat surface.

Supplementary Video S4: Climbing up to slopes.

Supplementary Video S5: Turning left and right using a tripod gait with the pneumatic turning part.

Supplementary Video S6: Crossing vertical obstacles.

Supplementary Video S7: Walking and rolling in a terrain environment that simulates a lava tube.

This work was supported by the National Key Research and Development Program of China (No. 2019YFB1309500), the National Natural Science Foundation of China (Grant No. 91948202 and Grant No. 51822502).

1 Zhuang H, Gao H, Deng Z et al. A review of heavy-duty legged robots. Sci China Tech Sci, 2014, 2: 298-314
2 Armour R H, Vincent J F V. Rolling in nature and robotics: a review. J Bionic Eng, 2006, 4: 195-208
3 Ding L, Gao H, Deng Z et al. Three-layer intelligence of planetary exploration wheeled mobile robots: robint, virtint, and humint. Sci China Tech Sci, 2015, 8: 1299-1317
4 Zhang Y, Li P, Quan J et al. Progress, challenges, and prospects of soft robotics for space applications. Adv Intell Syst, 2022, 2200071
5 Henschel J R. Spiders wheel to escape. S Afr J Sci, 1990, 3: 151-152
6 Lin H T, Leisk G G, Trimmer B. Goqbot: a caterpillar-inspired soft-bodied rolling robot. Bioinspir Biomim, 2011, 2: 26007
7 Western A, Haghshenas-Jaryani M, Hassanalian M. Golden wheel spider-inspired rolling robots for planetary exploration. Acta Astronaut, 2023, 34-48
8 Barstow J, Flores C E, Janney W et al. Bio-inspired autonomous robot with a novel mobility mechanism for planetary cave and lava tubes exploration. In, ed. AIAA SciTech Forum. 2022. 10
9 Li W, Guo X, Zhang W. SomBot: a bio-inspired dynamic somersaulting soft robot. Ieee Robot Autom Lett, 2021, 2: 1654-1661
10 Patel D K, Huang X, Luo Y et al. Highly dynamic bistable soft actuator for reconfigurable multimodal soft robots. Adv Mater Technol, 2023, 2: 2201259
11 Shah D S, Powers J P, Tilton L G et al. A soft robot that adapts to environments through shape change. Nat Mach Intell, 2020, 3: 51-59
12 Gkliva R, Kruusmaa M. Soft fluidic actuator for locomotion in multi-phase environments. IEEE Robot Autom Lett, 2022, 4: 10462-10469
13 Saranli U, Buehler M, Koditschek D E. Rhex: a simple and highly mobile hexapod robot. Int J Rob Res, 2001, 7: 616-631
14 Sadeghi A, Mondini A, Del Dottore E et al. Soft-legged wheel-based robot with terrestrial locomotion abilities. Front Robot Ai, 2016, 1-10
15 Ke X, Jang J, Chai Z et al. Stiffness preprogrammable soft bending pneumatic actuators for high-efficient, conformal operation. Soft Robot, 2022, 3: 613-624
16 Ke X, Zhang S, Chai Z et al. Flexible discretely-magnetized configurable soft robots via laser-tuned selective transfer printing of anisotropic ferromagnetic cells. Mater Today Phys, 2021, 100313
17 Bessone L, Sauro F, Maurer M et al. Testing technologies and operational concepts for field geology exploration of the moon and beyond; The esa pangaea-x campaign. Geophysical research abstracts, 2018, EGU2018-4013:

18 Nesnas I A, Kerber L, Parness A et al. Moon diver: A discovery mission concept for understanding the history of secondary crusts through the exploration of a lunar mare pit. In, ed. 2019 IEEE Aerospace Conference. Big Sky, MT, USA: IEEE, 2019. 1-23

19 Bell J, Redmond L, Carpenter K et al. Dynamic characterization of a pop-up folding flat explorer robot (PUFFER) for planetary exploration. In, ed Cham: Springer International Publishing, 2020. 383-391

20 SunSpiral V, Agogino AK, Atkinson D. Super Ball Bot—structures for planetary landing and exploration. NASA Innovative Advanced Concepts (NIAC) Program, Phase 2, Final Report. 2015. No. ARC-E-DAA-TN27344

21 Naclerio N D, Karsai A, Murray-Cooper M et al. Controlling subterranean forces enables a fast, steerable, burrowing soft robot. Sci Robot, 2021, 55: e2922

22 Ximenes S W, Elliott J O, Bannova O. Defining a mission architecture and technologies for lunar lava tube reconnaissance. In, ed. 13th ASCE Aerospace Division Conference on Engineering, Science, Construction, and Operations in Challenging Environments, and the 5th NASA/ASCE Workshop On Granular Materials in Space Exploration. 2012. 1-11

23 Xavier M S, Fleming A J, Yong Y K. Finite element modeling of soft fluidic actuators: overview and recent developments. Adv Intell Syst, 2020, 2000187

24 Armanini C, Boyer F, Mathew A T et al. Soft robots modeling: a structured overview. IEEE Trans Robot, 2023, 1-21

25 Hiller J, Lipson H. Dynamic simulation of soft multimaterial 3d-printed objects. Soft Robot, 2014, 1: 88-101

26 Gazzola M, Dudte L H, Mccormick A G et al. Forward and inverse problems in the mechanics of soft filaments. R Soc Open Sci, 2018, 6: 171628

27 Grazioso S, Di Gironimo G, Siciliano B. A geometrically exact model for soft continuum robots: the finite element deformation space formulation. Soft Robot, 2019, 6: 790-811

28 Lee K, Leong M C W, Chow M C K et al. Fem-based soft robotic control framework for intracavitary navigation. 2017 IEEE international Conference on Real-time Computing and Robotics (RCAR). Okinawa, Japan, July 14-18: IEEE, 2017. 11-16

29 Bieze T M, Largilliere F, Kruszewski A et al. Finite element method-based kinematics and closed-loop control of soft, continuum manipulators. Soft Robot, 2018, 3: 348-364

30 Ding L, Niu L, Su Y et al. Dynamic finite element modeling and simulation of soft robots. Chin J Mech Eng, 2022, 35: 24

31 Brodie E D. Salamander antipredator postures. Copeia, 1977, 3: 523-535

32 Garcia-Parfs M, Deban S M. A novel antipredator mechanism in salamanders rolling escape in hydromantes platycephalus. J Herpetol, 1995, 29: 149-151

33 Wu B, Xue Y, Ali I et al. The dynamic mortise-and-tenon interlock assists hydrated soft robots toward off-road locomotion. Research (Wash D C), 2022, 15

34 Wagner R V, Robinson M S. Distribution, formation mechanisms, and significance of lunar pits. Icarus, 2014, 52-60

35 Aguilar J, Zhang T N, Qian F F et al. A review on locomotion robophysics: the study of movement at the intersection of robotics, soft matter and dynamical systems. Rep Prog Phys, 2016, 11: 110001

36 Mosadegh B, Polygerinos P, Keplinger C et al. Pneumatic networks for soft robotics that actuate rapidly. Adv Funct Mater, 2014, 15: 2163-2170

37 Verma M S, Ainla A, Yang D et al. A soft tube-climbing robot. Soft Robot, 2018, 2: 133-137

38 Polygerinos P, Lyne S, Wang Z et al. Towards a soft pneumatic glove for hand rehabilitation. In, ed. 2013 IEEE/RSJ International Conference on Intelligent Robots and Systems. Tokyo, Japan: IEEE, 2013. 1512-1517

39 Ankaralı M M, Saranlı U. Control of underactuated planar pronking through an embedded spring-mass hopper template. Auton Robot, 2011, 2: 217-231

40 Marechal L, Balland P, Lindenroth L et al. Toward a common framework and database of materials for soft robotics. Soft Robot, 2021, 3: 284-297

41 Moseley P, Florez J M, Sonar H A et al. Modeling, design, and development of soft pneumatic actuators with finite element method. Adv Eng Mater, 2016, 6: 978-988

42 Ding L, Gao H, Deng Z et al. Foot–terrain interaction mechanics for legged robots: modeling and experimental validation. Int J Rob Res, 2013, 13: 1585-1606

43 Gao H, Jin M, Ding L et al. A real-time, high fidelity dynamic simulation platform for hexapod robots on soft terrain. Simul Model Pract Theory, 2016, 125-145

44 Hertz H. Ueber die berührung fester elastischer körper. crll, 1882, 92: 156-171

45 Liu Y, Xu K, Li J et al. Recurdyn multi-body dynamics simulation fundamentals applications and enhancements. Beijing: Publishing House of Electronics Industry, 2013. 296-298

46 Mcmordie D, Buehler M. Towards pronking with a hexapod robot. 4th Int. Conf. on Climbing and Walking Robots. 2001. 659-666